

PhaseNet: Phase-Encode Denoising Network for Compressed Sensing MRI

Marlon E. Bran Lorenzana, Shekhar S. Chandra and Feng Liu

Abstract—Sparse reconstruction is an important aspect of modern medical imaging, reducing the acquisition time of relatively slow modalities such as magnetic resonance imaging (MRI). Popular methods are based mostly on compressed sensing (CS), which relies on the random sampling of Fourier coefficients (k -space) to produce incoherent (noise-like) artefacts that can be removed via convex optimisation. Hardware constraints currently limit Cartesian CS to one dimensional (1D) phase-encode undersampling schemes, leading to coherent and structured artefacts. Reconstruction algorithms typically deploy an idealised and limited 2D regularisation for artefact removal, which increases the difficulty of image recovery. Recognising that phase-encode artefacts can be separated into contiguous 1D signals, we develop two decoupling techniques that enable explicit 1D regularisation. We thereby leverage the excellent incoherence characteristics in the phase-encode direction. We also derive a combined 1D + 2D reconstruction technique that further takes advantage of spatial relationships within the image, leading to an improvement of existing 2D deep-learned (DL) recovery techniques. Performance is evaluated on a brain and knee dataset. We find the proposed 1D CNN modules significantly improve PSNR and SSIM scores compared to the base 2D models, demonstrating a superior scaling of performance compared to increasing the size of 2D network layers.

Index Terms—CS, MRI, Aliasing, Phase-Encode

I. INTRODUCTION

The theory of compressed sensing (CS) [1], [2] is integral to sparse image reconstruction and has seen application in many areas of signal processing [3]. It is an especially important technology for medical applications, where scan times are significantly influenced by available sampling and reconstruction methods [4], [5]. Implementation of CS can therefore limit ionising radiation, improve temporal resolution and increase scanner availability. From a signal processing perspective, CS performs optimally when three conditions are met: incoherent

undersampling, transform sparsity and non-linear optimisation. Imaging problems will have unique considerations in these regards, most notably with respect to the sampling schemes available for each modality. For instance, magnetic resonance imaging (MRI) is an intrinsically lengthy process limited by physical and physiological constraints. Such constraints necessitate the sequential acquisition of k -space (discrete Fourier space) through continuous trajectories [6], [7]. As such, the undersampling strategy requires that sampled points are incoherent with respect to the regularising function, whilst adhering to magnetic resonance (MR) sampling characteristics. Over the past decade, there has been active development of both suitably incoherent sampling schemes for MRI, and the algorithms deployed in reconstruction.

Incoherence of a sampling matrix is often synonymous with orthogonal measurement and adhering to the well-known restricted isometry property (RIP) [8], [9]. The objective is to produce noise-like image artefacts that can be easily distinguished from image features. Ideal measurement is therefore non-deterministic or an approximation thereof, as random sampling has been shown to produce incoherence with high probability. Unfortunately for MR applications, pure random sampling is impractical to implement as a two-dimensional (2D) acquisition sequence [9], [10]. Instead, practical Cartesian CS fully samples in the frequency-encode direction (rows) and undersamples in the phase-encode direction (columns) [6], [7]. Incoherence between these measurements is thereby limited and 1D, which yields structured image artefacts along the undersampled axis. Strategies have been developed to mitigate this impact on image quality, such as varying the density of measurement [7], [11]. This is known as multi-level sampling, where acquisition is asymptotically coherent with the regularising function, ensuring that high energy regions of k -space are well captured [12], [13]. For reconstruction algorithms, another approach suggests first recovering an image from the undersampled 1D columns of k -space [14], fully exploiting randomness in the available direction.

Early reconstruction techniques utilised pre-defined sparsifying transforms for image regularisation, where undersampling artefacts remain noise-like and image features could be extracted [6], [15]. For successful implementation, these non-adaptive transforms rely on the sampling scheme to produce incoherent and unstructured artefacts. Adaptive methods instead learn the regularising function directly, ensuring a sparse representation throughout the reconstruction process [16]–[20]. However, general downsides to sparse encoding in-

This paragraph of the first footnote will contain the date on which you submitted your paper for review. It will also contain support information, including sponsor and financial support acknowledgment. For example, “This work was supported in part by the U.S. Department of Commerce under Grant BS123456.”

M. B. Lorenzana is with the School of Information Technology and Electrical Engineering, The University of Queensland, Brisbane Qld. 4072, Australia (e-mail: marlon.bran@uq.edu.au).

S. S. Chandra is with the School of Information Technology and Electrical Engineering, The University of Queensland, Brisbane Qld. 4072, Australia (e-mail: shekhar.chandra@uq.edu.au).

F. Liu is with the School of Information Technology and Electrical Engineering, The University of Queensland, Brisbane Qld. 4072, Australia (e-mail: feng@itee.uq.edu.au).

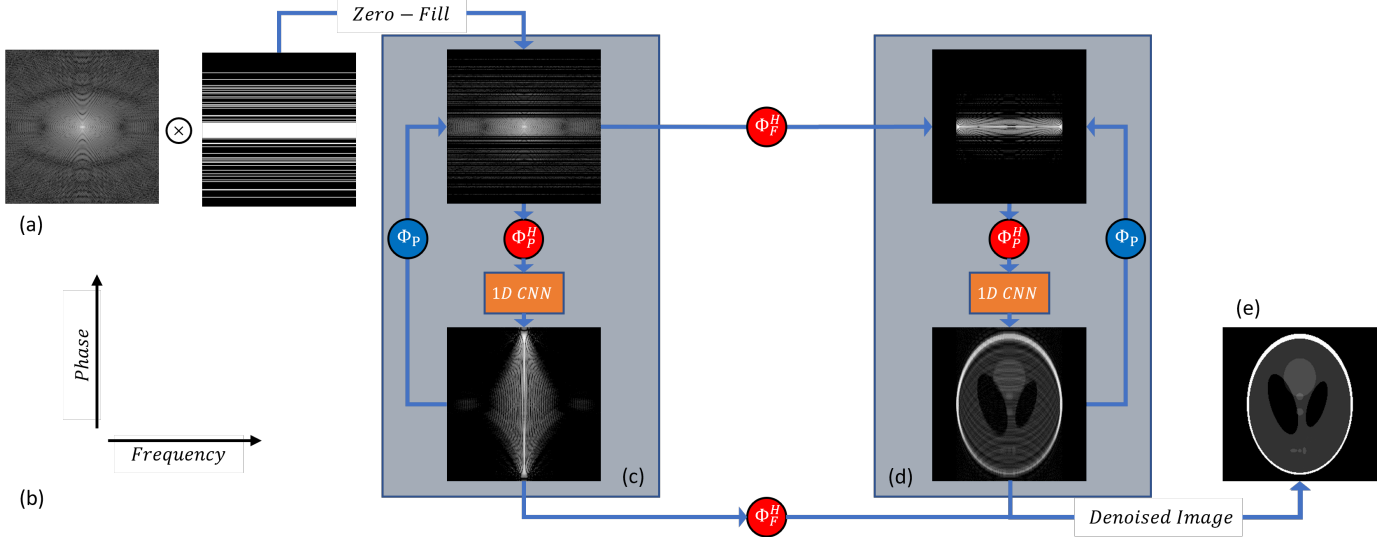


Fig. 1: The orange 1D CNN box is our proposed PhaseNet module designed to recover columns of aliased one-dimensional (1D) Fourier signals. Blue circles indicate the forward 1D DFT and red the inverse, with Φ_P and Φ_F specifying the phase- and frequency-encode directions respectively. (a) is the undersampling strategy, (b) the phase- and frequency-encode directions, (c) proposed denoising of 1D hybrid Fourier columns, (d) proposed denoising of 1D image columns, (e) the target image.

clude the introduction of additional image transformations, assumptions of image appearance, and necessitating increased calculations per iteration of CS [21]; learned sparse encoders exacerbate additive computation cost. Other prior knowledges have also been incorporated into the recovery process, such as a low-ranked constraint [22], [23], or redundancies in multi-coil MRI [24]–[27]. Machine learning elevated this notion of learned regularisation by expressing CS-MRI solutions as deep neural networks (DNN). Their data-driven approach allows for task-specific, highly non-linear operations that consistently outperform conventional CS recovery techniques [28]. For the most part, deep-learned (DL) methods operate in the image domain, with k -space measurements integrated into the loss function [29] or data consistency layer [30]–[36]. Alternatively, k -space interpolation networks [37], [38] or direct k -space to image transformation [39], [40] have also been proposed. As CS-MRI artefacts degrade an image in non-local and potentially unrecoverable ways, recent contributions have instead proposed a dual-domain reconstruction approach. These networks execute operations in k -space alongside image denoising layers, enabling recovery of image features that may be otherwise lost from single-domain techniques. Some explore k -space recovery in the denoising sense [41]–[44], and others perform k -space interpolation via k -space redundancies [45]–[47]. Although dual-domain networks excel at recovering images from random 2D Cartesian and projection-based undersampling patterns, they typically deploy convolutional neural network (CNN) operations directly in k -space. Reconstruction is thereby limited to interpolation from known values, with large distances between sampled points necessitating elaborate network architectures and high computation costs to overcome.

In this paper, we employ a series of 1D CS operations that efficiently populate missing k -space for 1D Cartesian random

undersampling. This regularisation is performed by 1D CNN modules, providing an improved estimate of k -space before 2D reconstruction. Similar DL formulations have been proposed, such as domain-transform manifold learning in phase-encoding direction [40] and One-dimensional Deep Low-rank and Sparse Network [47]. To the best of our knowledge, however, this is the first 1D only network designed to supplement existing 2D reconstruction techniques. Our contributions are summarised as follows:

- A general 1D CS framework for MRI that decouples undersampled k -space into a series of 1D signals in two separate domains. Asymptotic coherence between sampling and regularisation is improved by explicitly recovering missing data in the direction of undersampling.
- Development of an efficient proximal mapping for DL non-linear regularisers in our proposed algorithm. This constitutes the proposed 1D DNN regularisation modules.
- Combination of our 1D modules with existing 2D DL recovery methods efficiently achieves image quality superior to simply increasing the size of the original network.
- Comparisons with state-of-the-art dual-domain reconstruction techniques highlight that our CS-based recovery of missing k -space is better suited to phase-encode undersampling MRI.

The proposed method is a **Phase** reconstruction **NET**work (PhaseNet) that enhances the regularisation of 1D undersampled MRI. After presenting relevant theory and mathematical derivations, the proposed method is described in Section II. Experiments with a purely 1D reconstruction, as well as integrating the model into well-known networks Deep cascade of Convolutional Neural Networks (DcCNN) [30] and Iterative Shrinkage-Thresholding Algorithm Network (ISTA-Net) [32] are investigated. Finally, Section IV contains a discussion of these experiments.

II. METHODS

A. Compressed Sensing

One can model CS for MRI by considering an object MR image \mathbf{x}_0 and the subset of associated k -space measurements \mathbf{y} , such that $\mathbf{y} = R\mathbf{F}\mathbf{x}_0 + \sigma$. Here \mathbf{F} represents the 2D discrete Fourier transform (DFT), R is the undersampling matrix and σ is complex Gaussian noise. As equation $\mathbf{x} = (R\mathbf{F})^H [\mathbf{y} - \sigma]$ is ill-posed, image estimate \mathbf{x} can be recovered according to,

$$\arg \min_{\mathbf{x}} \|\mathbf{R}\mathbf{F}\mathbf{x} - \mathbf{y}\|_2^2 + \rho h(\mathbf{x}), \quad (1)$$

where $h(\cdot)$ is a regularisation function. Commonly, $h(\cdot)$ is chosen such that $\rho h(\mathbf{x}) = \rho \|\Psi\mathbf{x}\|_1$, which enforces sparsity in some transform Ψ . As incoherence between sampling and sparsifying functions is important for successful implementation of CS [12], [13], it can be beneficial to consider the limitations of available sampling schemes when selecting the regularisation employed. In this work, we explore the addition of explicit DL 1D regularisation for phase-encode undersampled MRI.

B. Decoupling 2D k -space into 1D signals

To leverage the excellent 1D incoherence characteristics of phase-encode undersampling, we must decouple image \mathbf{x} and its k -space \mathbf{y} into contiguous 1D signals. We identify two possible formulations of the problem by considering the following equality,

$$\mathbf{y} = \mathbf{F}\mathbf{x} = \Phi_P \mathbf{x} \Phi_F. \quad (2)$$

Φ_F and Φ_P are the 1D DFT in the frequency- (rows) and phase-encode (columns) direction respectively. We may then relate columns of \mathbf{x} and \mathbf{y} with the following two equations,

$$(\mathbf{y}\Phi_F^H)_n = (\Phi_P \mathbf{x})_n \quad (3)$$

$$(\Phi_P^H \mathbf{y})_n = (\mathbf{x}\Phi_F)_n, \quad (4)$$

where n denotes the n^{th} column. Recognising that artefacts arising from phase-encode undersampling can be characterised as 1D perturbations of Eq. 3, Yang et al. [14] provide an “upgraded” image estimate before 2D CS. Their proposed optimisation problem can be expressed as,

$$\min_{\mathbf{x}} \sum_n \|\mathbf{R}_{1D}(\Phi_P \mathbf{x})_n - (\mathbf{y}\Phi_F^H)_n\|_2^2 + \rho \mathbf{TV}_{1D}(\mathbf{x}_n), \quad (5)$$

\mathbf{R}_{1D} is the 1D undersampling pattern. As visualised in Fig. 1d, 1D columns \mathbf{x}_n are related to Fourier measurements $(\mathbf{y}\Phi_F^H)_n$ via the 1D DFT. Therefore, recovery of missing k -space is possible by enforcing a total-variation (TV) constraint on columns \mathbf{x}_n , whilst ensuring consistency with related measurements $(\mathbf{y}\Phi_F^H)_n$. Alternatively, if we consider Eq. 4, one could just as easily pose the following optimisation problem,

$$\min_{\mathbf{x}} \sum_n \|\mathbf{R}_{1D}(\Phi_P \mathbf{x}\Phi_F)_n - \mathbf{y}_n\|_2^2 + \rho h_{1D}((\mathbf{x}\Phi_F)_n) \quad (6)$$

In this instance, k -space values will be populated by enforcing constraint $h(\cdot)$ on aliased 1D signals of intermediate domain $\mathbf{x}\Phi_F$ (Fig. 1c). For simplicity, we instead define,

$$G(\mathbf{u}, \mathbf{v}) = \|\mathbf{R}_{1D}\Phi_P \mathbf{u} - \mathbf{v}\|_2^2 + \rho h_{1D}(\mathbf{u}), \quad (7)$$

which allows Eqs. 5 and 6 to be written concisely for each method as $G(\mathbf{x}_n, (\mathbf{y}\Phi_F^H)_n)$ and $G((\mathbf{x}\Phi_F)_n, \mathbf{y}_n)$ respectively. Expressing Eq. 7 in this manner highlights that arbitrary regularisers $h_{1D}(\cdot)$, which are suitably incoherent with respect to \mathbf{y} in image \mathbf{x} and intermediate $\mathbf{x}\Phi_F$ domain can be deployed for image recovery.

C. Phase-Encode Alias Artefact Suppression

Algorithm 1: 1D Iterative Update

Result: Recover \mathbf{u}_0 from measurements \mathbf{v}

Function: $\arg \min_{\mathbf{u}} \|\mathbf{R}_{1D}\Phi_P \mathbf{u} - \mathbf{v}\|_2^2 + \rho h_{1D}(\mathbf{u})$

Parameters:

- n_t - Number of iterations
- ρ_t - Regularisation strength
- $h(\cdot)$ - Indicator function of noiseless \mathbf{u}

Init: Set $t = 0$, $\mathbf{u}^0 = \Phi_P^H \mathbf{v}$

while $t \leq n_t$ **do**

$$\mathbf{z}^t = \mathbf{R}_{1D}\Phi_P \mathbf{u}^{t-1} - \mathbf{v} \quad (8)$$

$$\mathbf{r}^t = \mathbf{u}^{t-1} - \rho^t \Phi_P^H \mathbf{z}^t \quad (9)$$

$$\mathbf{u}^t = \arg \min_{\mathbf{u}} \|\mathbf{u} - \mathbf{r}^t\|_2^2 + h(\mathbf{u}) \quad (10)$$

end

To efficiently suppress 1D artefacts, we propose to solve Eq. 7 via the proximal gradient descent technique described by Algorithm 1. In this approach, the fully sampled 1D signal \mathbf{u}_0 is recovered from measurements \mathbf{v} by enforcing $h(\mathbf{u})$ in each iteration. If $h(\cdot)$ is an indicator function of set C , where C is the set of noiseless MRI for which a family of denoisers $g(\cdot)$ exist, then Eq. 10 is a special case of proximal mapping where $\mathbf{u} = \text{prox}_h(\mathbf{r})$, and therefore,

$$\mathbf{u}^t = \arg \min_{\mathbf{u} \in C} \|\mathbf{u} - \mathbf{r}^t\|_2^2 = g(\mathbf{r}^t). \quad (11)$$

This assumes that $\mathbf{u}^{t-1} - \rho^t \Phi_P^H \mathbf{z}^t$ can be modelled as $\mathbf{u}_0 + \nu^t$, where ν^t is residual undersampling noise. We propose to replace $g(\cdot)$ with $g_{cnn}(\cdot|\theta_t)$, which allows for a data-driven mapping between noisy measurements $\mathbf{u}_0 + \nu^t$ and the fully sampled image \mathbf{u}_0 . Eq. 10 can therefore be written as,

$$\mathbf{u}^t = g_{cnn}(\mathbf{r}^t|\theta_t), \quad (12)$$

here θ_t are the CNN parameters at iteration t . Fig. 2a illustrates our chosen architecture for $g(\cdot|\theta_t)$, which features a skip connection for residual learning. As discussed in [32], [38], residuals of natural images are highly compressible, consisting mainly of high frequency components. Given our proposed $g_{cnn}(\cdot|\theta_t)$ is applied directly to \mathbf{r}^t , we deploy this residual architecture to encourage sparsity in the output signal. As the 1D regularisation is intended to complement existing 2D reconstruction algorithms, $g(\cdot|\theta_t)$ is composed of just 3 1D CNN operations with intermediate Leaky ReLU activation functions. The kernel size is 9 and the feature size is 8. Therefore, each iteration of Algorithm 1 requires just 885 parameters, yielding a lightweight 1D regularisation module. Fig. 2b illustrates the update process outlined in Algorithm 1.

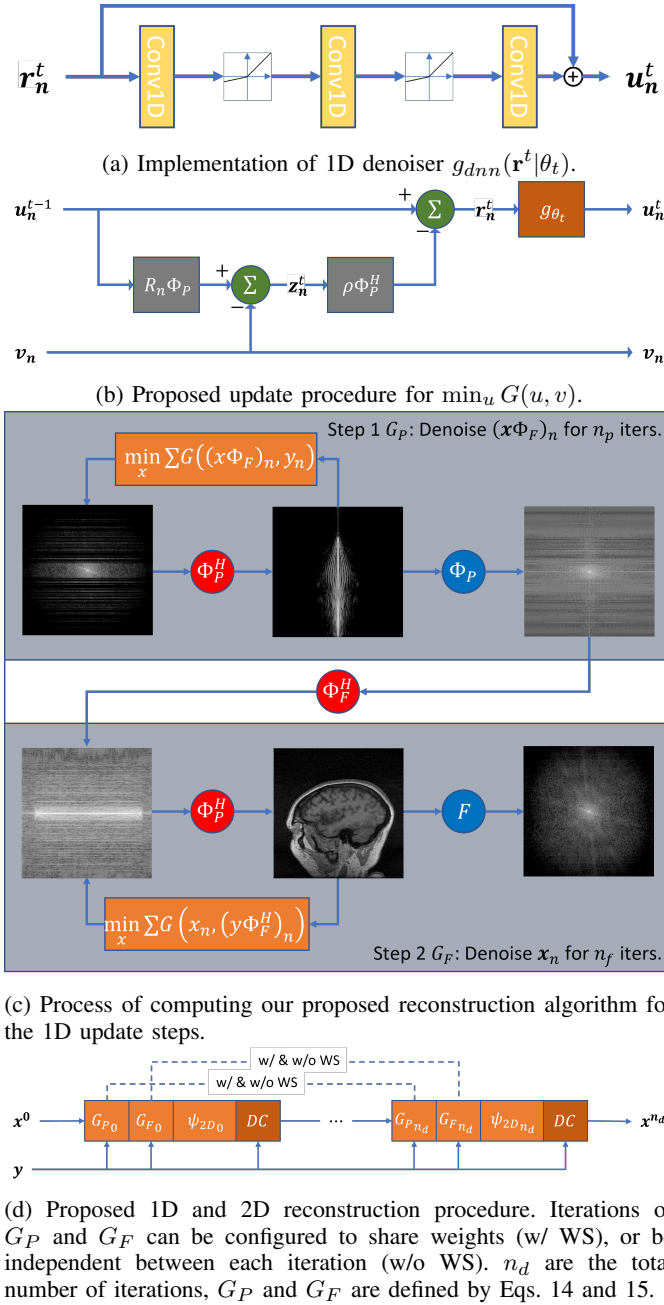


Fig. 2: 1D proximal gradient descent technique for accelerated phase-encode MRI.

D. Combining 1D and 2D Regularisation

1) *Motivation*: Many existing DL CS-MRI algorithms are dependent on image domain operations, only integrating k -space information into data consistency layers and loss function design. Two major limitations have been identified with this approach. Firstly, undersample artefacts are structured and non-local, obscuring image features in potentially unrecoverable ways [43]. Secondly, the exact sampling scheme is not considered as part of the reconstruction process, therefore limiting regularisation to an idealised 2D transformation. Recent state-of-the-art contributions have explored dual-domain architectures, executing convolutional operations

directly in k -space. For example, Dual-Domain Recurrent Network (DuDoRNet) [43] solves the non-local problem by invoking a sophisticated, Dilated Residual Dense Network (DRD-Net) with a large receptive field. When applied to k -space, DRD-Net attempts to recover missing samples by interpolating from captured information. Whilst effective, this design is computationally expensive. Further, it does not directly address the structured nature of CS-MRI artefacts. This is particularly evident for phase-encode undersampling, where artefacts can be decoupled into 1D signals. In our proposed optimisation problem, Eq. 12 recovers 1D signal \mathbf{u}_0 from estimate \mathbf{r}^t , assuming it can be modelled as $\mathbf{r}^t = \mathbf{u}_0 + \nu^t$. Because phase-encode undersampling is incoherent with respect to \mathbf{r}^t , it is expected that ν^t can be modelled as signal independent and noise-like [14], [47]. For this reason, we propose to combine our 1D CS recovery method with existing 2D CS algorithms. The combined regularisation ensures 1D perturbations are directly penalised. Further, for each $N \times M$ image there will be M 1D training samples available, ensuring additional parameters incurred are well-trained. We demonstrate superior scaling with a total number of parameters compared to simply increasing the size of the original 2D network. We also compare against DuDoRNet in various tests. Despite being more computationally efficient, our combined 1D + 2D networks consistently outperform alternatives.

2) *Implementation*: In the general case, we define our combined 1D and 2D optimisation problem as follows,

$$\min_{\mathbf{x}} \|\mathbf{R}\mathbf{F}\mathbf{x} - \mathbf{y}\|_2^2 + \lambda \Psi_{2D}(\mathbf{x}) + \rho \sum_n G((\mathbf{x}\Phi_F)_n, \mathbf{y}_n) + \mu \sum_n G(\mathbf{x}_n, (\mathbf{y}\Phi_F^H)_n) \quad (13)$$

where $\mu \sum_n G(\mathbf{x}_n, (\mathbf{y}\Phi_F^H)_n)$ and $\rho \sum_n G((\mathbf{x}\Phi_F)_n, \mathbf{y}_n)$ penalise perturbations in columns of image \mathbf{x} and intermediate domains $\mathbf{x}\Phi_F$, $\lambda \Psi_{2D}(\mathbf{x})$ is the 2D regularisation. The combined alternating minimisation (AM) procedure can be split into three steps.

Step 1: Populate missing k -space measurements by denoising \mathbf{x} in intermediate domain $\mathbf{x}\Phi_F$,

$$G_P = \min_{\mathbf{x}} \rho \sum_n G((\mathbf{x}\Phi_F)_n, \mathbf{y}_n). \quad (14)$$

Step 2: Using this upgraded estimate of k -space we denoise image columns \mathbf{x}_n by solving,

$$G_F = \min_{\mathbf{x}} \mu \sum_n G(\mathbf{x}_n, (\mathbf{y}\Phi_F^H)_n). \quad (15)$$

Steps 1 and 2 can be solved in the proximal gradient descent technique described in Section II-C and illustrated in Fig. 2c. The steps will be defined as solving G_P and G_F respectively. The number of iterations each is computed for is n_p and n_f .

Step 3: The 2D regularisation can be any existing DL model by setting $\Psi_{2D}(\cdot)$ to the appropriate regulator. For instance, regularisation in the denoising sense as per DcCNN [30],

$$\Psi_{2D}(\mathbf{x}) = \|\mathbf{x} - f_{cnn}(\mathbf{x} | \theta_f)\|_2^2, \quad (16)$$

or regularisation by transformation sparsity as per ISTA-Net [32],

$$\Psi_{2D}(\mathbf{x}) = \|\mathcal{R}(\mathbf{x})\|_1. \quad (17)$$

In fact, 2D regularisation can even be defined by dual-domain algorithms such as MRI dual-domain reconstruction network (MD-Recon-Net) [44] or DuDoRNet [43]. Fig. 2d illustrates our 1D regularisation combined with a general 2D regularisation for reference. Here, n_d are the total number of iterations to solve the AM algorithm described in this section.

3) Loss Function: Because we perform reconstruction in multiple image domains, we found it beneficial to explicitly supervise k -space, intermediate domains, and image space:

$$L = \|\mathbf{x}_0 - \hat{\mathbf{x}}\|_1 + \tau_k \|\mathbf{y}_0 - \hat{\mathbf{y}}\|_1 + \tau_f \|\mathbf{y}_0 \Phi_F^H - \hat{\mathbf{y}} \Phi_F^H\|_1 + \tau_p \|\Phi_P^H \mathbf{y}_0 - \Phi_P^H \hat{\mathbf{y}}\|_1 \quad (18)$$

Here, \mathbf{x}_0 and \mathbf{y}_0 are the target image and associated k -space measurements, $\hat{\mathbf{x}}$ and $\hat{\mathbf{y}}$ are the estimated image and k -space. Additionally, τ_k , τ_f , τ_p are the k -space, intermediate Φ_F and Φ_P domain loss ratios. These are set to 0.1, 0.3, and 0.3.

III. RESULTS AND DISCUSSION

A. Experimental Configuration

Two public MR datasets have been used to train and test our proposed model, each featuring raw 2D k -space data of three-dimensional (3D) volumes. Magnitudes of all 3D volumes were normalised between $[0, 1]$. There was no overlap between training, validation or test sets. Single-coil images are obtained with emulated single-coil methodology as-per each dataset's implementation [48], [49].

1) Calgary-Campinas: We use the *Calgary-Campinas* brain dataset [48] to investigate the behaviour of our proposed 1D regularisation technique in several ablation studies. The dataset consists of 45 fully-sampled T1-w volumes acquired from a 12-channel clinical MR scanner (Discovery MR750; General Electric (GE) Healthcare, Waukesha, WI). In total, there are 7654 slices. Training consists of 25 subjects and 4254 slices. Validation and test each consist of 10 subjects and 1700 slices. The matrix size is 256×256 .

2) FastMRI: We also train and test on a subset of the NYU fastMRI single-coil knee dataset [49], [50]. In this study, we utilise the 3 Tesla coronal proton density (PD)-weighted images without fat suppression. This dataset consists of 12,366 slices from 332 subjects, captured on one of three clinical 3T MR scanners (Siemens Magnetom Skyra, Prisma and Biograph mMR). The data was acquired from a 15-channel knee coil array. Training consists of 8293 slices from 223 volumes. The validation set contains 2081 slices from 56 volumes. The test set is 1992 slices from 53 volumes. The matrix size is 320×320 .

3) Training Methodology: Discrete Fourier space was sampled using a 1D Gaussian random mask. We use power signal-to-noise ratio (PSNR) and structural similarity (SSIM) to evaluate closeness to the original image. All experiments were conducted on an NVIDIA SXM-2T V100 graphics processing unit (GPU) with 32GB of vRAM. All networks were implemented in PyTorch and trained using the Adam

TABLE I: Number of unique 1D PhaseNet layers with respect to 2D update steps n_d . Iterations n_f and n_p relate to 1D minimisation problems G_P (Eq. 14) and G_F (Eq. 15), respectively.

PhaseNet + 5 2D layers				
	n_p	n_f	n_d	1D Layers
Shared	1	5	5	6
Un-Shared				30
				1D Params
				5298
				26,490

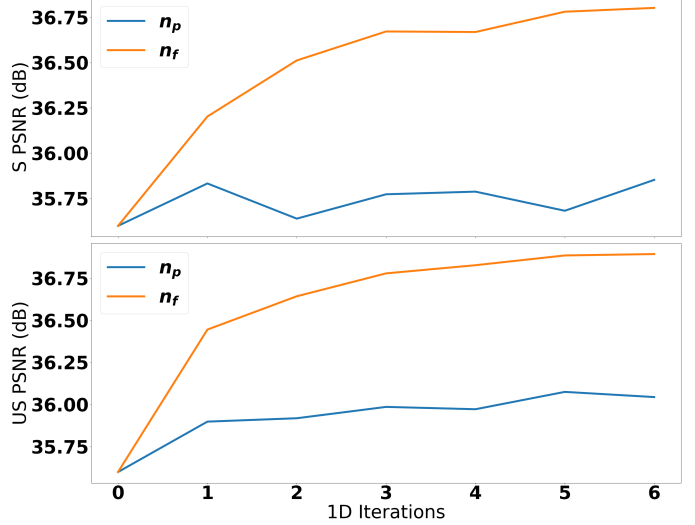


Fig. 3: Scaling of the PhaseNet layers combined with DcCNN configured to $D5C5$ ($n_d = 5$). n_p and n_f are iterations of G_P (Eq. 14) and G_F (Eq. 15) respectively. Dataset used is Calgary-Campinas at a reduction factor of 4.

optimiser. All DcCNN and ISTA-Net implementations were trained with a learning rate of 10^{-4} , a batch size of 10 and with custom loss function Eq. 18; ISTA-Net also had matrix inverse loss as per [32]. DuDoRNet and MD-Recon-Net were trained following the original implementations [43], [44], with batch sizes of 5 and 10 respectively. However, we reduced the number of residual dense blocks (RSD) from 3 to 2 within each DRD-Net layer when training on the knee dataset. This is due to the knee dataset being substantially larger than the brain dataset, where 3 (RSD) will require several weeks to complete just 200 epochs. In contrast, it takes 1 day for our proposed DcCNN + 1D network to converge. Additionally, our network features approximately $3\times$ fewer parameters compared to DuDoRNet, meaning the reduced model is a closer comparison. All networks were trained until convergence, where the network with the lowest validation loss was chosen for testing.

B. Ablation Studies

To establish a relationship between iterations of G_P and G_F to reconstruction quality, we explore the combination of our proposed 1D PhaseNet modules with the 2D regularisation found in DcCNN [30] and ISTA-Net [32]. As per the AM algorithm described in Section II-D.2 and Fig. 2d, the 1D recovery is interleaved between 2D steps. We also experiment with shared and un-shared configurations. Here, shared 1D modules indicate that the weights of iterations of G_P and G_F

TABLE II: Average reconstruction performance for the Calgary-Campinas brain dataset. Included in this table are the number of parameters for tested networks. **Bold** and underlined indicate best and second-best outcomes, respectively. $P1F5$ shows that $n_p = 1$ and $n_f = 5$ for G_P and G_F , respectively. Shared and unshared relate to the 1D weights in-between 2D denoising steps. The increase in parameters is with respect to the baseline model without modification (top row of DcCNN and ISTA-Net+).

Method	Conv Layers	DC Layers	2D Filters	1D Layers	R=2		R=3		R=4		% Increase Parameters
					PSNR	SSIM	PSNR	SSIM	PSNR	SSIM	
DcCNN	5	5	32	0	42.78	0.98	38.44	0.95	35.60	0.93	–
	5	5	38	0	42.87	0.98	38.47	0.95	35.68	0.93	39.9
	6	5	32	0	42.91	0.98	37.81	0.95	35.98	0.93	32.0
	5	7	32	0	43.07	0.98	38.98	0.95	36.30	0.93	40.0
DcCNN P1F5 (Shared)	5	5	32	6	<u>43.42</u>	0.98	<u>39.46</u>	0.96	<u>36.84</u>	0.94	3.6
DcCNN P1F5 (UnShared)	5	5	32	30	43.45	0.98	39.55	0.96	36.94	0.94	<u>18.2</u>
ISTA-Net+	6	5	32	0	42.85	0.98	38.59	0.95	35.96	0.93	–
	6	5	38	0	38.83	0.98	38.38	0.95	35.93	0.93	40.2
	6	7	32	0	43.11	0.98	39.15	0.95	36.42	0.93	40.0
ISTA-Net+ P1F5 (Shared)	5	5	32	6	<u>43.38</u>	0.98	<u>39.44</u>	0.96	<u>36.75</u>	0.94	2.8
ISTA-Net+ P1F5 (UnShared)	5	5	32	30	43.45	0.98	39.55	0.96	36.95	0.94	<u>13.8</u>

Fig. 4: Reconstruction performance demonstrated at R3 (top) and R4 (bottom) reduction factor of sagittal cross-sectional brain MR image, with the zoomed area (red rectangle) highlighting regions where reconstruction performance is notably improved by PhaseNet layers. DcCNN [30] and ISTA-Net [32] are the references. PS and P indicate the inclusion of PhaseNet in shared and un-shared configurations. Values $\in [0, 1]$.

are common in-between 2D update steps. Alternatively, un-shared means that every 1D iteration is unique throughout the reconstruction. Table I compares the total number of unique 1D layers necessary for shared and un-shared configurations given iterations of G_P (n_p) and G_F (n_f).

1) Scaling: Fig. 3 compares the relative scaling between iterations of G_P (n_p) and G_F (n_f) in both shared (top) and un-shared (bottom) configurations, combined with a reference DcCNN network [30]. DcCNN is configured with 5 data consistency layers, 5 convolutional layers and 32 filters per convolution (D5C5). Experiments are conducted at $R = 4$. It is noticeable that G_F achieves superior PSNR scores on the test-set, converging at $n_f = 5$. This suggests that convolutions applied in image space are more effective than the intermediate domain denoising of G_P . We also note that G_F in shared configuration provides similar PSNR scores to un-shared. On

the other hand, shared G_P layers do not benefit from $n_p > 1$. For simplicity, all subsequent experiments will combine G_P and G_F layers by fixing $n_p = 1$ and $n_f = 5$ as per Table I.

2) Comparison to Large Versions: Using the $n_p = 1$, $n_f = 5$ configuration, we compare the performance of DcCNN and ISTA-Net boosted with PhaseNet layers against larger versions of the original networks. The objective is to demonstrate that PhaseNet enables better scaling with a total number of parameters compared to simply increasing the size of the original network. Average reconstruction performance is summarised in Table II, where the first rows of DcCNN and ISTA-Net are the baseline models. Subsequent rows then increase network size by either increasing the number of filters, increasing the number of cascaded convolutions and in the instance of DcCNN, increasing the number of convolutional layers in each 2D denoising step. The PhaseNet models are equivalent to

TABLE III: Average reconstruction performance for the Calgary-Campinas brain dataset. Included are the number of parameters for tested networks and associated training information. **Bold** and underlined indicate best and second-best outcomes respectively. DcCNN and ISTA-Net+ with $P1F5$ are PhaseNet boosted with $n_p = 1$ and $n_f = 5$ for G_P and G_F .

Method	R=2		R=4		R=6		R=8		Number of Parameters	Minutes Per Epoch
	PSNR	SSIM	PSNR	SSIM	PSNR	SSIM	PSNR	SSIM		
DcCNN	42.78	0.98	35.60	0.93	32.69	0.89	30.51	0.85	145.6K	0.9
ISTA-Net+	42.87	0.98	35.68	0.93	32.95	0.89	30.67	0.85	191.5K	1.6
MD-Recon-Net	42.91	0.98	35.79	0.93	32.74	0.89	30.38	0.85	289.3K	1.3
DuDoRNet	43.02	0.98	36.24	0.93	33.18	0.90	30.71	0.85	649.4K	13.2
DcCNN	43.42	0.98	36.84	0.94	33.44	0.90	30.98	0.86	150.9K	2.0
PIF5 (Shared)										
DcCNN	43.45	0.98	36.94	0.94	33.53	0.90	<u>31.05</u>	0.86	172.1K	2.1
PIF5 (Unshared)										
ISTA-Net+	43.38	0.98	36.75	0.94	33.47	0.90	<u>31.05</u>	0.86	196.8K	2.5
PIF5 (Shared)										
ISTA-Net+	43.45	0.98	36.95	0.94	33.57	0.91	31.09	0.86	218.0K	2.6
PIF5 (Unshared)										

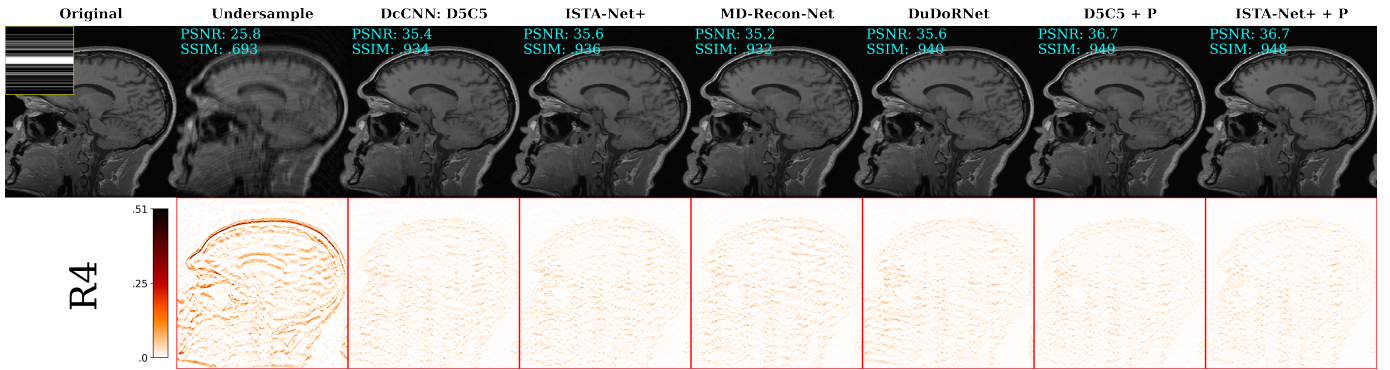


Fig. 5: Reconstruction performance demonstrated at R4 reduction factor. Featured in this comparison are the baseline single-domain DcCNN configured as $D5C5$, ISTA-Net+, dual-domain networks MD-Recon-Net and DuDoRNet, and the PhaseNet boosted DcCNN and ISTA-Net+ implementations without weight sharing. Values $\in [0, 1]$.

baseline models with 1D regularisation interleaved between 2D denoising steps. While the shared configuration uses the same $n_p + n_f = 6$ 1D modules between each 2D denoising step, the un-shared networks deploy $(n_p + n_f) \times n_d = 30$.

For both DcCNN and ISTA-Net and at all reduction factors, the inclusion of PhaseNet as an additional 1D regularisation achieves the best PSNR and SSIM scores. This feat is particularly notable for the shared configuration, where only 3.6% and 2.8% of additional parameters are necessary for DcCNN and ISTA-Net respectively. Fig. 4 illustrates the benefits afforded by PhaseNet for two sample images. It is noted in the error maps that noise-like and faint image features are easily lost by the undersampling, most evidently at R4. We see the contrast between white and grey matter is better preserved by PhaseNet implementations, highlighted in the locations of red and blue arrows.

C. Vs State-of-the-art algorithms

To further explore PhaseNet, we compare against state-of-the-art dual-domain reconstruction techniques DuDoRNet [43] and MD-Recon-Net [44] using the Calgary-Campinas brain and fastMRI knee datasets. As with the ablation study, baseline DcCNN and ISTA-Net networks are also included.

1) *Calgary Campinas Brain*: Fig. 5 compares reconstruction methods for a sample image of the Calgary-Campinas Brain dataset. The figure shows PhaseNet versions of DcCNN and

ISTA-Net yield the highest PSNR and SSIM scores. Compared to the state-of-the-art method DuDoRNet, we improve the reconstruction of the test image from 35.6dB to 36.7dB. The error map image reflects this PSNR advantage. Our findings are also observed in Table III, which contains each network's average performance at multiple acceleration factors. Surprisingly, adding just 3.6% and 2.8% PhaseNet parameters to DcCNN and ISTA-Net respectively, the networks can outperform MD-Recon-Net and DuDoRNet. Further, at higher reduction factors (R6 and R8), MD-Recon-Net cannot improve the reconstruction compared to the baseline DcCNN and ISTA-Net. We suspect this is due to large distances between sampled points in k -space limiting the utility of convolutions. DuDoRNet on the other hand, retains a performance advantage throughout due to the large receptive field within its DRD-Net modules. It should be noted that the loss function used for MD-Recon-Net is simply mean-squared error (MSE) as per [44], whereas all DcCNN and ISTA-Net implementations are trained using Eq. 18. DuDoRNet also employs a sophisticated loss function [43].

2) *fastMRI Knee*: For the knee images, the frequency and phase-encode directions are transposed to columns and rows respectively. Sample reconstructions at R6 and R8 are demonstrated in Fig. 6. We see again that the PhaseNet boosted networks outperform the base DcCNN and ISTA-Net implementations. In fact, we also see that the PSNR and SSIM

TABLE IV: Average reconstruction performance for the fastMRI knee dataset. Included in this table are the number of parameters for tested networks and associated training information. **Bold** and underline indicate the best and second-best outcomes, respectively. DcCNN and ISTA-Net+ with P1F5 are PhaseNet boosted with $n_p = 1$ and $n_f = 5$ for G_P and G_F .

Method	R=2		R=4		R=6		R=8		Number of Parameters	Minutes Per Epoch
	PSNR	SSIM	PSNR	SSIM	PSNR	SSIM	PSNR	SSIM		
DcCNN	35.38	0.87	32.22	0.76	30.67	0.70	29.14	0.64	145.6K	3.6
ISTA-Net+	35.39	0.87	32.23	0.76	30.73	0.70	29.22	0.65	191.5K	6.5
MD-Recon-Net	35.37	0.87	32.21	0.76	30.64	0.70	28.98	0.64	289.3K	6.1
DuDoRNet	35.44	0.87	32.32	0.76	30.87	0.70	29.54	0.65	452.3K	465
DcCNN	35.37	0.87	32.32	0.76	30.88	0.70	29.42	0.65	150.9K	5.7
PIF5 (Shared)	35.39	0.87	32.23	0.76	30.73	0.70	29.22	0.65	191.5K	6.5
DcCNN	<u>35.43</u>	0.87	32.35	0.76	<u>30.93</u>	0.70	<u>29.45</u>	0.65	172.1K	7.1
PIF5 (Unshared)	35.41	0.87	<u>32.33</u>	0.76	30.91	0.70	29.44	0.65	196.8K	9.5
ISTA-Net+ PIF5 (Shared)	<u>35.43</u>	0.87	32.35	0.76	30.95	0.70	29.54	0.65	218.0K	9.5
ISTA-Net+ PIF5 (Unshared)	<u>35.43</u>	0.87	32.35	0.76	30.95	0.70	29.54	0.65	218.0K	9.5

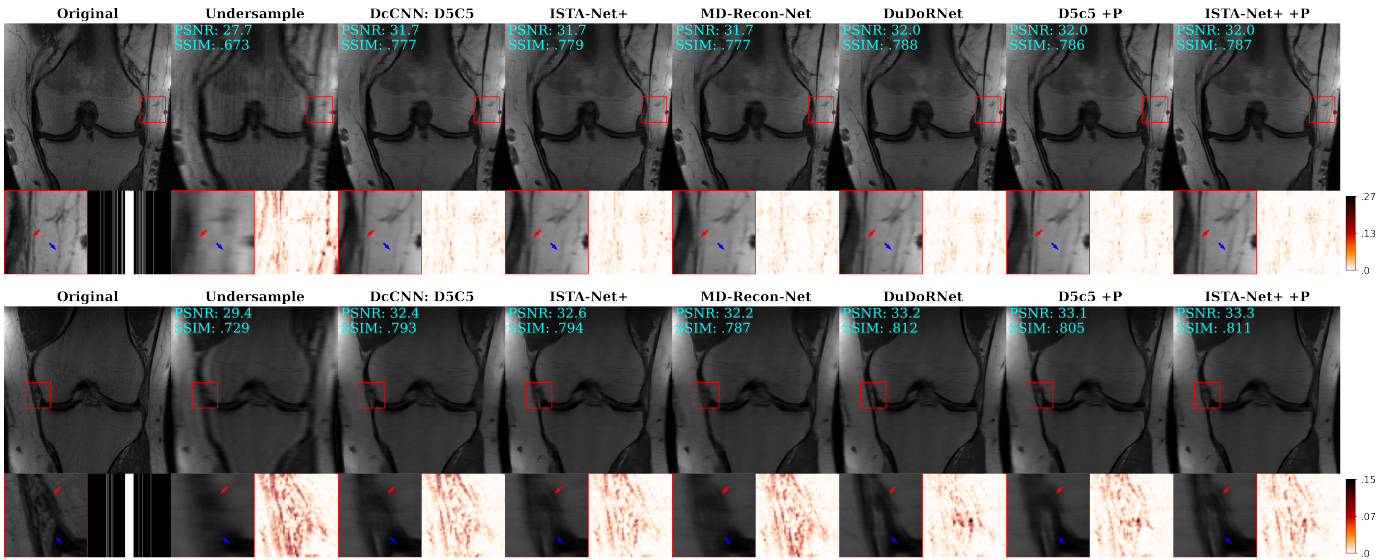


Fig. 6: Reconstruction performance demonstrated at R6 (top) and R8 (bottom) reduction factor of cross-sectional knee MR image, with the zoomed area (red rectangle) highlighting regions where the reconstruction is notably improved by PhaseNet layers. DcCNN [30] and ISTA-Net [32] are the reference. P indicates the inclusion of PhaseNet in an un-shared configuration. Values $\in [0, 1]$.

scores have become competitive with DuDoRNet. This is an important outcome, as DuDoRNet required approximately 41 days to complete 130 epochs on the 8293 knee slices. As both DcCNN and ISTA-Net employ relatively simple network architectures, and the proposed PhaseNet modules are designed to supplement the 2D reconstruction, the boosted networks require just 23 hours for convergence. This suggests that our approach to regularise phase-encode undersampling artefacts in the direction of undersampling provides a more efficient model from which to recover an MR image.

D. 1D Only Reconstruction

Recently, Wang et al. explored a fully 1D CNN to recover multi-coil phase-encode undersampled MRI [47]. The network achieves state-of-the-art performance when the number of training samples is limited, with performance that remains competitive to 2D techniques as the training samples are increased. The problem posed is similar to that solved in our G_F (Eq. 15), with an additional low-rank constraint

to interpolate missing k -space from captured values. Our approach differs from this in three key forms. Firstly, their low-rank constraint is applied directly to $\mathbf{y}\Phi_F^H$, which we only utilise for data consistency in $G(\mathbf{x}_n, (\mathbf{y}\Phi_F^H)_n)$ (G_F). Secondly, they do not consider 1D aliasing artefacts present in $\mathbf{x}\Phi_F$ that we denoise in $G((\mathbf{x}\Phi_F)_n, \mathbf{y}_n)$ (G_P). Lastly, PhaseNet was developed to supplement existing DL 2D solvers and, therefore, features a minimal number of parameters. We therefore investigate the suitability of PhaseNet modules for 1D-only reconstruction. In this configuration, the 1D layers illustrated in Fig. 2 have been scaled into a 687.2K parameter, 1D-only network. Here, the number of 1D convolution layers per iteration has been increased from 3 to 6, the number of filters per layer from 8 to 32, and n_p and n_f have been set to 5 and 13. The number of parameters is similar to [47]. For simplicity, we continue to experiment with single-coil MRI; this is easily extended to multi-coil by combining each reconstructed image with the square root of the sum of squares. Fig. 7 compares the PhaseNet 1D reconstruction, the 2D

TABLE V: Comparison between a large 1D only PhaseNet, a 2D only reconstruction via DcCNN configured in *D5C7* and the combined 1D + 2D reconstruction configured as *P1F5* + *D5C5*. Dataset is Calgary-Campinas.

Method	R=4		Number of Parameters
	PSNR	SSIM	
PhaseNet P3F15	35.74	0.93	687.2K
D7C5	36.30	0.93	203.8.6K
D5C5 P1F5	36.94	0.94	172.1K

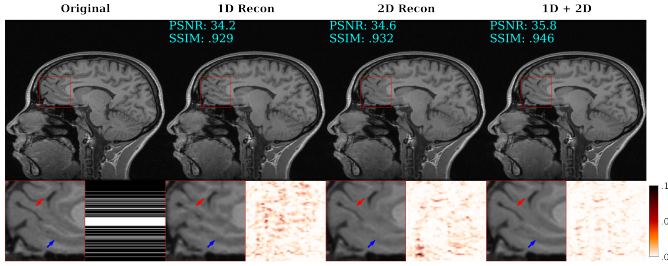


Fig. 7: Comparison of 1D, 2D and combined 1D + 2D reconstructions for the Calgary-Campinas brain dataset at R4. 1D is our PhaseNet only, 2D is DcCNN configured to *D5C7* and 1D + 2D is PhaseNet combined with *D5C5*.

reconstruction from DcCNN configured in a larger *D5C7* and a combined 1D + 2D reconstruction (2D network is *D5C5*). We find competitive reconstruction performance between 1D and 2D techniques, with PSNR scores only $0.4dB$ apart. The combined reconstruction however is $1.2dB$ higher. As per the difference image and the regions indicated by the red and blue arrows, the combined reconstruction better captures image features that are otherwise lost or corrupted in the alternative reconstructions.

We suggest that extension of PhaseNet to multi-coil MRI should include the low-rank constraint, such that the reconstruction benefits from standard 2D regularisation, as-well-as 1D regularisation of columns of image \mathbf{x} (G_F), our proposed 1D regularisation of columns in intermediate domain $\mathbf{x}\Phi_F$ (G_P) and the low-rank constraint on columns of intermediate domain $\Phi_P\mathbf{x}$ as suggested by Wang *et al.* [47].

IV. CONCLUSION

In this work, we have introduced two novel regularisation layers for phase-encode undersampled MRI that enhance the reconstruction ability of existing 2D reconstruction techniques. This proposed PhaseNet regularisation leverages the excellent 1D incoherence properties of phase-encode undersampled MRI in two hybrid Fourier domains. The combined 1D and 2D regularisation better models image artefacts, producing superior performance scaling compared to simply increasing the size and number of 2D layers in the original network. In fact, increasing model size by just 3 – 4% improves the reconstruction of DcCNN and ISTA-Net to above state-of-the-art dual-domain networks such as MD-Recon-Net and DuDoRNet. We have also found competitive performance from a completely 1D reconstruction network based on PhaseNet, potentially enabling high-quality reconstruction for data-constrained appli-

cations. In our experiments, image quality benefited more from the proposed image-domain regularisation of G_F (Eq. 15) than hybrid Fourier regulariser of G_P (Eq. 14). However, their combination serves to boost image quality further.

While the objective of this work is to improve existing reconstruction techniques, we suggest a joint 1D and 2D reconstruction strategy be developed that limits the necessary data consistency (DC) layers within each denoising iteration. In the implementation investigated in this paper, we require a 1D DC layer for each 1D PhaseNet module. This results from the AM approach to joint 1D and 2D reconstruction. While this solution yields simple construction and compatibility with existing 2D networks, it is inefficient to perform many fast Fourier transform (FFT) operations. As such, it may be useful to select and un-roll an optimisation method that limits the number of necessary DC operations.

Another avenue to be explored is the 1D reconstruction of undersampled projection data, wherein missing sinogram projections are populated via an approach similar to our proposed hybrid Fourier G_P .

REFERENCES

- [1] E. Candes, J. Romberg, and T. Tao, “Robust uncertainty principles: exact signal reconstruction from highly incomplete frequency information,” *IEEE Transactions on Information Theory*, vol. 52, no. 2, pp. 489–509, Feb. 2006.
- [2] D. Donoho, “Compressed sensing,” *IEEE Transactions on Information Theory*, vol. 52, no. 4, pp. 1289–1306, Apr. 2006.
- [3] M. F. Duarte and Y. C. Eldar, “Structured Compressed Sensing: From Theory to Applications,” *IEEE Transactions on Signal Processing*, vol. 59, no. 9, pp. 4053–4085, Sep. 2011.
- [4] C. G. Graff and E. Y. Sidky, “Compressive sensing in medical imaging,” *Applied Optics*, vol. 54, no. 8, p. C23, Mar. 2015.
- [5] M. Sandilya and S. Nirmala, “Compressed sensing trends in magnetic resonance imaging,” *Engineering Science and Technology, an International Journal*, vol. 20, no. 4, pp. 1342–1352, Aug. 2017.
- [6] M. Lustig, D. Donoho, and J. M. Pauly, “Sparse MRI: The application of compressed sensing for rapid MR imaging,” *Magnetic Resonance in Medicine*, vol. 58, no. 6, pp. 1182–1195, 2007.
- [7] M. Lustig, D. Donoho, J. Santos, and J. Pauly, “Compressed Sensing MRI,” *IEEE Signal Processing Magazine*, vol. 25, no. 2, pp. 72–82, Mar. 2008.
- [8] E. J. Candès, “The restricted isometry property and its implications for compressed sensing,” *Comptes Rendus Mathématique*, vol. 346, no. 9–10, pp. 589–592, May 2008.
- [9] A. Majumdar, *Compressed Sensing for Magnetic Resonance Image Reconstruction*, 1st ed. Cambridge University Press, Feb. 2015.
- [10] S. Geethanath, R. Reddy, A. S. Konar, S. Imam, R. Sundaresan, R. B. D. R., and R. Venkatesan, “Compressed Sensing MRI: A Review,” *Critical Reviews in Biomedical Engineering*, vol. 41, no. 3, pp. 183–204, 2013.
- [11] M. Seeger, H. Nickisch, R. Pohmann, and B. Schölkopf, “Optimization of k -space trajectories for compressed sensing by Bayesian experimental design: Bayesian Optimization of k -Space Trajectories,” *Magnetic Resonance in Medicine*, vol. 63, no. 1, pp. 116–126, Jan. 2010.
- [12] F. Krahmer and R. Ward, “Stable and Robust Sampling Strategies for Compressive Imaging,” *IEEE Transactions on Image Processing*, vol. 23, no. 2, pp. 612–622, Feb. 2014.
- [13] B. Adcock, A. C. Hansen, C. Poon, and B. Roman, “BREAKING THE COHERENCE BARRIER: A NEW THEORY FOR COMPRESSED SENSING,” *Forum of Mathematics, Sigma*, vol. 5, p. e4, 2017.
- [14] Y. Yang, F. Liu, Z. Jin, and S. Crozier, “Aliasing Artefact Suppression in Compressed Sensing MRI for Random Phase-Encode Undersampling,” *IEEE Transactions on Biomedical Engineering*, vol. 62, no. 9, pp. 2215–2223, Sep. 2015.
- [15] S. Ramani and J. A. Fessler, “Parallel MR Image Reconstruction Using Augmented Lagrangian Methods,” *IEEE Transactions on Medical Imaging*, vol. 30, no. 3, pp. 694–706, Mar. 2011.

- [16] S. Ravishanker and Y. Bresler, "MR Image Reconstruction From Highly Undersampled k-Space Data by Dictionary Learning," *IEEE Transactions on Medical Imaging*, vol. 30, no. 5, pp. 1028–1041, May 2011.
- [17] —, "Sparsifying transform learning for Compressed Sensing MRI," in *2013 IEEE 10th International Symposium on Biomedical Imaging*, Apr. 2013, pp. 17–20.
- [18] X. Qu, Y. Hou, F. Lam, D. Guo, J. Zhong, and Z. Chen, "Magnetic resonance image reconstruction from undersampled measurements using a patch-based nonlocal operator," *Medical Image Analysis*, vol. 18, no. 6, pp. 843–856, Aug. 2014.
- [19] W. Dong, G. Shi, X. Li, Y. Ma, and F. Huang, "Compressive Sensing via Nonlocal Low-Rank Regularization," *IEEE Transactions on Image Processing*, vol. 23, no. 8, pp. 3618–3632, Aug. 2014.
- [20] Z. Zhan, J.-F. Cai, D. Guo, Y. Liu, Z. Chen, and X. Qu, "Fast Multiclass Dictionaries Learning With Geometrical Directions in MRI Reconstruction," *IEEE Transactions on Biomedical Engineering*, vol. 63, no. 9, pp. 1850–1861, Sep. 2016.
- [21] B. Wen, S. Ravishanker, L. Pfister, and Y. Bresler, "Transform Learning for Magnetic Resonance Image Reconstruction: From Model-Based Learning to Building Neural Networks," *IEEE Signal Processing Magazine*, vol. 37, no. 1, pp. 41–53, Jan. 2020.
- [22] J. P. Haldar, "Low-Rank Modeling of Local k-Space Neighborhoods (LORAKS) for Constrained MRI," *IEEE Transactions on Medical Imaging*, vol. 33, no. 3, pp. 668–681, Mar. 2014, conference Name: IEEE Transactions on Medical Imaging.
- [23] X. Zhang, H. Lu, D. Guo, Z. Lai, H. Ye, X. Peng, B. Zhao, and X. Qu, "Accelerated MRI Reconstruction With Separable and Enhanced Low-Rank Hankel Regularization," *IEEE Transactions on Medical Imaging*, vol. 41, no. 9, pp. 2486–2498, Sep. 2022.
- [24] K. P. Pruessmann, M. Weiger, M. B. Scheidegger, and P. Boesiger, "SENSE: Sensitivity encoding for fast MRI," *Magnetic Resonance in Medicine*, vol. 42, no. 5, pp. 952–962, 1999.
- [25] M. A. Griswold, P. M. Jakob, R. M. Heidemann, M. Nittka, V. Jellus, J. Wang, B. Kiefer, and A. Haase, "Generalized autocalibrating partially parallel acquisitions (GRAPPA)," *Magnetic Resonance in Medicine*, vol. 47, no. 6, pp. 1202–1210, 2002, eprint: <https://onlinelibrary.wiley.com/doi/pdf/10.1002/mrm.10171>.
- [26] M. Lustig and J. M. Pauly, "SPIRiT: Iterative self-consistent parallel imaging reconstruction from arbitrary k-space," *Magnetic Resonance in Medicine*, vol. 64, no. 2, pp. 457–471, 2010, eprint: <https://onlinelibrary.wiley.com/doi/pdf/10.1002/mrm.22428>.
- [27] J. Zhang, C. Liu, and M. E. Moseley, "Parallel Reconstruction Using Null Operations (PRUNO)," *Magnetic resonance in medicine : official journal of the Society of Magnetic Resonance in Medicine / Society of Magnetic Resonance in Medicine*, vol. 66, no. 5, pp. 1241–1253, Nov. 2011.
- [28] S. S. Chandra, M. Bran Lorenzana, X. Liu, S. Liu, S. Bollmann, and S. Crozier, "Deep learning in magnetic resonance image reconstruction," *Journal of Medical Imaging and Radiation Oncology*, vol. 65, no. 5, pp. 564–577, 2021.
- [29] G. Yang, S. Yu, H. Dong, G. Slabaugh, P. L. Dragotti, X. Ye, F. Liu, S. Arridge, J. Keegan, Y. Guo, and D. Firmin, "DAGAN: Deep De-Aliasing Generative Adversarial Networks for Fast Compressed Sensing MRI Reconstruction," *IEEE Transactions on Medical Imaging*, vol. 37, no. 6, pp. 1310–1321, Jun. 2018.
- [30] J. Schlemper, J. Caballero, J. V. Hajnal, A. Price, and D. Rueckert, "A Deep Cascade of Convolutional Neural Networks for MR Image Reconstruction," in *Information Processing in Medical Imaging*, M. Niethammer, M. Styner, S. Aylward, H. Zhu, I. Oguz, P.-T. Yap, and D. Shen, Eds. Cham: Springer International Publishing, 2017, vol. 10265, pp. 647–658.
- [31] K. Hammernik, T. Klatzer, E. Kobler, M. P. Recht, D. K. Sodickson, T. Pock, and F. Knoll, "Learning a variational network for reconstruction of accelerated MRI data," *Magnetic Resonance in Medicine*, vol. 79, no. 6, pp. 3055–3071, 2018.
- [32] J. Zhang and B. Ghanem, "ISTA-Net: Interpretable Optimization-Inspired Deep Network for Image Compressive Sensing," in *2018 IEEE/CVF Conference on Computer Vision and Pattern Recognition*, Jun. 2018, pp. 1828–1837.
- [33] Y. Yang, J. Sun, H. Li, and Z. Xu, "ADMM-CSNet: A Deep Learning Approach for Image Compressive Sensing," *IEEE Transactions on Pattern Analysis and Machine Intelligence*, vol. 42, no. 3, pp. 521–538, Mar. 2020.
- [34] T. Lu, X. Zhang, Y. Huang, D. Guo, F. Huang, Q. Xu, Y. Hu, L. Ou-Yang, J. Lin, Z. Yan, and X. Qu, "pFISTA-SENSE-ResNet for parallel MRI reconstruction," *Journal of Magnetic Resonance (San Diego, Calif.: 1997)*, vol. 318, p. 106790, Sep. 2020.
- [35] B. Zhou, J. Schlemper, N. Dey, S. S. Mohseni Salehi, K. Sheth, C. Liu, J. S. Duncan, and M. Sofka, "Dual-domain self-supervised learning for accelerated non-Cartesian MRI reconstruction," *Medical Image Analysis*, vol. 81, p. 102538, Oct. 2022.
- [36] M. B. Lorenzana, C. Engstrom, and S. S. Chandra, "Transformer Compressed Sensing Via Global Image Tokens," in *2022 IEEE International Conference on Image Processing (ICIP)*. Bordeaux, France: IEEE, Oct. 2022, pp. 3011–3015.
- [37] M. Akçakaya, S. Moeller, S. Weingärtner, and K. Ugurbil, "Scan-specific robust artificial-neural-networks for k-space interpolation (RAKI) reconstruction: Database-free deep learning for fast imaging," *Magnetic Resonance in Medicine*, vol. 81, no. 1, pp. 439–453, 2019.
- [38] Y. Han, L. Sunwoo, and J. C. Ye, "k-Space Deep Learning for Accelerated MRI," *IEEE Transactions on Medical Imaging*, vol. 39, no. 2, pp. 377–386, Feb. 2020.
- [39] B. Zhu, J. Z. Liu, S. F. Cauley, B. R. Rosen, and M. S. Rosen, "Image reconstruction by domain-transform manifold learning," *Nature*, vol. 555, no. 7697, pp. 487–492, Mar. 2018.
- [40] T. Eo, H. Shin, Y. Jun, T. Kim, and D. Hwang, "Accelerating Cartesian MRI by domain-transform manifold learning in phase-encoding direction," *Medical Image Analysis*, vol. 63, p. 101689, Jul. 2020.
- [41] T. Eo, Y. Jun, T. Kim, J. Jang, H. Lee, and D. Hwang, "KIKI-net: cross-domain convolutional neural networks for reconstructing undersampled magnetic resonance images," *Magnetic Resonance in Medicine*, vol. 80, no. 5, pp. 2188–2201, Nov. 2018.
- [42] R. Souza, R. M. Lebel, and R. Frayne, "A Hybrid, Dual Domain, Cascade of Convolutional Neural Networks for Magnetic Resonance Image Reconstruction," in *Proceedings of The 2nd International Conference on Medical Imaging with Deep Learning*, ser. Proceedings of Machine Learning Research, M. J. Cardoso, A. Feragen, B. Glocker, E. Konukoglu, I. Oguz, G. Unal, and T. Vercauteren, Eds., vol. 102. PMLR, Jul. 2019, pp. 437–446.
- [43] B. Zhou and S. K. Zhou, "DuDoRNet: Learning a Dual-Domain Recurrent Network for Fast MRI Reconstruction With Deep T1 Prior," in *2020 IEEE/CVF Conference on Computer Vision and Pattern Recognition (CVPR)*. Seattle, WA, USA: IEEE, Jun. 2020, pp. 4272–4281.
- [44] M. Ran, W. Xia, Y. Huang, Z. Lu, P. Bao, Y. Liu, H. Sun, J. Zhou, and Y. Zhang, "MD-Recon-Net: A Parallel Dual-Domain Convolutional Neural Network for Compressed Sensing MRI," *IEEE Transactions on Radiation and Plasma Medical Sciences*, vol. 5, no. 1, pp. 120–135, Jan. 2021.
- [45] A. Sriram, J. Zbontar, T. Murrell, C. L. Zitnick, A. Defazio, and D. K. Sodickson, "GrappaNet: Combining Parallel Imaging With Deep Learning for Multi-Coil MRI Reconstruction," in *2020 IEEE/CVF Conference on Computer Vision and Pattern Recognition (CVPR)*. Seattle, WA, USA: IEEE, Jun. 2020, pp. 14 303–14 310.
- [46] Z. Ke, W. Huang, Z.-X. Cui, J. Cheng, S. Jia, H. Wang, X. Liu, H. Zheng, L. Ying, Y. Zhu, and D. Liang, "Learned Low-Rank Priors in Dynamic MR Imaging," *IEEE Transactions on Medical Imaging*, vol. 40, no. 12, pp. 3698–3710, Dec. 2021, conference Name: IEEE Transactions on Medical Imaging.
- [47] Z. Wang, C. Qian, D. Guo, H. Sun, R. Li, B. Zhao, and X. Qu, "One-dimensional Deep Low-rank and Sparse Network for Accelerated MRI," *IEEE Transactions on Medical Imaging*, pp. 1–1, 2022.
- [48] R. Souza, O. Lucena, J. Garrafa, D. Gobbi, M. Saluzzi, S. Appenzeller, L. Rittner, R. Frayne, and R. Lotufo, "An open, multi-vendor, multi-field-strength brain MR dataset and analysis of publicly available skull stripping methods agreement," *NeuroImage*, vol. 170, pp. 482–494, Apr. 2018.
- [49] J. Zbontar, F. Knoll, A. Sriram, T. Murrell, Z. Huang, M. J. Muckley, A. Defazio, R. Stern, P. Johnson, M. Bruno, M. Parente, K. J. Geras, J. Katsnelson, H. Chandarana, Z. Zhang, M. Drozdal, A. Romero, M. Rabbat, P. Vincent, N. Yakubova, J. Pinkerton, D. Wang, E. Owens, C. L. Zitnick, M. P. Recht, D. K. Sodickson, and Y. W. Lui, "fastMRI: An Open Dataset and Benchmarks for Accelerated MRI," Dec. 2019, arXiv:1811.08839 [physics, stat].
- [50] F. Knoll, J. Zbontar, A. Sriram, M. J. Muckley, M. Bruno, A. Defazio, M. Parente, K. J. Geras, J. Katsnelson, H. Chandarana, Z. Zhang, M. Drozdal, A. Romero, M. Rabbat, P. Vincent, J. Pinkerton, D. Wang, N. Yakubova, E. Owens, C. L. Zitnick, M. P. Recht, D. K. Sodickson, and Y. W. Lui, "fastMRI: A Publicly Available Raw k-Space and DICOM Dataset of Knee Images for Accelerated MR Image Reconstruction Using Machine Learning," *Radiology: Artificial Intelligence*, vol. 2, no. 1, p. e190007, Jan. 2020, publisher: Radiological Society of North America.